Carbon Particle In-Situ Alloying of the Case-Hardening Steel 16MnCr5 in Laser Powder Bed Fusion

Matthias Schmitt [1,*], Albin Gottwalt [2], Jakob Winkler [3], Thomas Tobie [3], Georg Schlick [1], Karsten Stahl [3], Ulrich Tetzlaff [2], Johannes Schilp [1] and Gunther Reinhart [1]

[1] Fraunhofer Institute for Casting, Composite and Processing Technology IGCV, 86159 Augsburg, Germany; georg.schlick@igcv.fraunhofer.de (G.S.); johannes.schilp@igcv.fraunhofer.de (J.S.); gunther.reinhart@igcv.fraunhofer.de (G.R.)

[2] Faculty of Mechanical Engineering, Technical University of Applied Sciences Ingolstadt, 85049 Ingolstadt, Germany; Albin.Gottwalt@thi.de (A.G.); ulrich.tetzlaff@thi.de (U.T.)

[3] Institute of Machine Elements—Gear Research Centre (FZG), Technical University of Munich, 85748 Garching, Germany; j.winkler@fzg.mw.tum.de (J.W.); tobie@fzg.mw.tum.de (T.T.); stahl@fzg.mw.tum.de (K.S.)

[*] Correspondence: matthias.schmitt@igcv.fraunhofer.de; Tel.: +49-821-9067-8147

Abstract: The carbon content of steel affects many of its essential properties, e.g., hardness and mechanical strength. In the powder bed fusion process of metals using a laser beam (PBF-LB/M), usually, pre-alloyed metal powder is solidified layer-by-layer using a laser beam to create parts. A reduction of the carbon content in steels is observed during this process. This study examines adding carbon particles to the metal powder and in situ alloying in the PBF-LB/M process as a countermeasure. Suitable carbon particles are selected and their effect on the particle size distribution and homogeneity of the mixtures is analysed. The workability in PBF-LB is then shown. This is followed by an evaluation of the resulting mechanical properties (hardness and mechanical strength) and microstructure in the as-built state and the state after heat treatment. Furthermore, potential use cases like multi-material or functionally graded parts are discussed.

Keywords: additive manufacturing; PBF-LB/M; in situ alloying; case-hardening steel; 16MnCr5; gears; multi-material

1. Introduction and Literature Review

Additive manufacturing (AM) refers to a category of production techniques that can produce complex parts [1]. Powder Bed Fusion of metals using a laser beam (PBF-LB/M, according to ISO 52900) is one of the most advanced technologies in the field of AM and is commonly used in industry. Other commonly used names and abbreviations are selective laser melting (SLM) or laser powder bed fusion (L-PBF). However, for standardization, the terminology according to ISO5299 is applied. PBF-LB/M is capable of producing parts with very detailed features from metal powder [2]. During the process, a thin layer of metal powder is solidified by a laser beam to create one layer of the part. The complete part is created through layer-by-layer fabrication [3]. This process opens up the possibility of producing parts with complex shapes and internal features, which cannot be accomplished by conventional manufacturing methods. At the same time, the production of small lot sizes becomes economical since little or no tooling is needed [1,4]. Combining these benefits leads to the development of new business models [4]. PBF-LB/M processes metals and focuses predominantly on a small number of alloys like tool or corrosion-resistant steels (e.g., maraging steel, 316L or 17-4PH), titanium alloys (Ti-6Al-4V) and nickel-based alloys (e.g., IN718 and IN625) [5]. Nevertheless, other material classes such as case hardening steels are also investigated [6]. This material class is mainly used in drive train applications because of its high wear resistance and high fatigue load-carrying capacity [7]. Case hardening steels have a carbon content of 0.15–0.23 wt.%. During the case hardening

treatment of parts, the carbon content in the case is increased to 0.8–1.0 wt.% through the diffusion of carbon gas. Quenching results in a high case hardness of about 60 HRC and a comparably lower core hardness with good dynamic and ductile fatigue properties [8].

In 2014, the basic workability of 16MnCr5 (1.7131) for PBF-LB/M was presented by Kamps and Reinhart, claiming that a relative density of close to 100% can be achieved using an M1 system from Concept Laser [9]. Ziebura and Meiners stated the workability of 16MnC5 and 42CrMo4 in 2016, though without specifying the parameters used and the resulting mechanical properties [10]. Kluge et al. showed that the similar case hardening steel 20MnCr5 (1.7147) can be used to fabricate drive train applications [11]. However, no detailed parameters for the PBF-LB/M process such as laser power or scan speed were published. The focus of Kluge et al. was on measuring the resulting distortion with different base plate temperatures and combinations of different stress relief annealing procedures. Increasing the base plate temperature led to a decrease in distortion, measured by cantilevers. Stress relief annealing proved effective in reducing distortion to almost zero, no matter which base plate temperature was used [11]. Schmitt et al. published a detailed processing approach and examined a process window for four selected energy density levels for 16MnCr5 in PBF-LB/M [6]. The influence of scan strategies and energy density on the resulting hardness of specimens with high relative densities (>99.8%) was discussed, but no clear correlation could be derived. The full process chain (PBF-LB/M, stress relief annealing, machining, case hardening and hard machining) for parts made from case hardened steels was investigated by Kamps [12]. The high cooling rates in PBF-LB/M (c.f. [13]) between 4 and 40 K/µs lead to martensitic or bainitic microstructures, which are closely connected to the carbon content during the cooling process, as described by Kamps during the evaluation of the as-built state [12]. The static mechanical properties after PBF-LB/M and the dynamic behaviour of finished gears from 16MnCr5 were compared to values derived from conventional manufacturing and showed that static properties can be met and that the load-carrying capacity was nearly reached [12]. Beer et al. processed the case hardening steel M50NiL, which is used for ball bearings with a relative density of above 99.9%. Experiments were conducted on the case hardening capabilities and showed that a case hardness of more than 750 HV can be achieved [14]. The design potentials in gears manufactured by PBF-LB/M were examined, showing that the integration of cooling channels can greatly decrease flank temperatures under high loads [15]. Kamps and Schmitt [12,16] examined the benefits of introducing lightweight design in parts such as gears made from case hardening steels. In both cases, mass savings of more than 30% were demonstrated, which could increase the drivetrain efficiency. Nevertheless, the complex process chain of case hardened parts (e.g., state of residual stress or distortion) has to be evaluated in more detail since the interdependencies between the PBF-LB/M process and the heat treatment for lightweight structures are not well known yet.

One issue with the PBF-LB/M process is that the chemical composition of the built part often does not match the chemical composition of the metal powder that is used. This phenomenon of element depletion has been observed during the processing of the corrosion resistant steel 316L (1.4404), which resulted in a decrease in chromium and manganese from the powder to the resulting part [17]. At the same time, the carbon content of the resulting process fume was analysed and showed a much higher percentage by weight of carbon than expected from the low carbon steel. A study was performed in 2009 into the processing of four low-alloyed steel powders with varying carbon content from 0.33 to 1.04 wt.% [18]. The resulting carbon loss was highest in the steel with 1.04 wt.%, even though the energy density required for full solidification was low compared to the energy density needed for the 0.33 wt.% carbon steel. Taha et al. described the loss of carbon during the processing of ultra-high carbon steel in PBF-LB/M [19]. The carbon content from powder to part decreased by 0.12 wt.%. Jelis et al. studied the carbon content during powder reuse when processing AISI 4340 steel and showed that more than 15% of the carbon content was lost after two recycling stages [20]. Higher carbon decarburization is described for the martensitic stainless steel AISI 420, which showed a loss of 21% carbon

during the PBF-LB/M process [21]. The authors explain the depletion with the reaction of carbon and residual oxygen in the build chamber. Additionally, carbon-rich zones at the melt pool boundaries are shown. Comparably low hardness values were observed in the core when examining the case hardening properties of 20MnCr5 samples [11]. This could be the result of carbon depletion, which leads to a lower hardenability. Beer et al. conducted measurements along the process chain from raw material to powder and part for the case hardening steel M50NiL. They concluded that the carbon content decreased from the raw material to the powder during the atomization process and an additional decrease of carbon content was observed during the PBF-LB/M process [14].

Carbon is a main alloying element to achieve wear resistant properties in steels and leads to a martensitic microstructure. Carbon atoms are around half the size of iron atoms, making them interstitially soluble. They can diffuse with relative ease within unoccupied space, e.g., the octahedron gaps. The diffusion direction is determined by concentration differences that can be described by Fick's law. The formation of martensite in particular leads to an increase in hardness. This is caused by a diffusion-free process from austenite, whereby the carbon in the martensite is forcibly dissolved. Subcooling is needed for this folding process to take place, which can occur during quenching or in processes with high cooling rates such as laser hardening or L-PBPF. One property determined by the carbon content is the hardness. The maximum hardness that can be achieved depending on the carbon content is calculated by Equation (1) for un- and low alloyed steels when the carbon range is between 0.1 and 0.6 wt.% [22]:

$$\text{Hardness}_{max} = 32.87 + 83.86 \times (\text{wt.\% C}) - 49.75 \times (\text{wt.\% C})^2 \text{ HRC} \tag{1}$$

Hence, a drop in the carbon content during PBF-LB/M is closely linked to the resulting microstructure and a lower achievable hardness. Furthermore, hardenability is related to the distortion that takes place during case hardening [23]. During case hardening, the core hardness is determined by the initial carbon content because carbon diffusion only takes place in the case region. During PBF-LB/M, the carbon depletion of case hardening steels could be compensated by longer carburization times, even though the core material would not be affected. Furthermore, this would lead to a change in the hardness profile and the resulting case hardening depth (CHD), which has very narrow tolerances in certain component requirements, e.g., gears [24]. Therefore, requirements have to be met to expand the field of application for PBF-LB/M. Possible strategies can be to increase the carbon content in specially alloyed powders to counteract the depletion or to add carbon particles to commercially available powders, also referred to as in situ alloying. The first strategy requires many iterations of powder atomization, which is costly and time-consuming. These development costs can only be compensated by large production series and a valid business case. In contrast, in situ alloying is a flexible and cost-efficient strategy that allows fast iterations [25]. Further applications of carbon-modified powders are functionally graded materials, hybrid processes or multi-material PBF-LB/M [26,27].

Murali et al. published a study on processing a mixture of pure iron and graphite powder with PBF-LB/M using a carbon content of 0.8 wt.%. The manufactured specimen only reached a relative density of around 90%. Hardness measurements in a range from 350 HV to 540 HV showed an inhomogeneous dissolution of the carbon [28]. Additionally, Simchi and Pohl processed a mixture of pure iron and graphite with varying carbon contents from 0.4 to 1.6 wt.%. A layer thickness of 0.1 mm was used in the PBF-LB/M process. Increasing the carbon content led to a better densification and improved the surface quality. Nevertheless, a maximum relative density of only around 80% was achieved [29]. Kruth et al. used a mixture of Fe, Ni, Cu and Fe3P powders and a modified laser mode as well as scanning patterns. A density of 91% was ultimately achieved [30]. In more recent studies, Zhang et al. used a powder mix of Fe-80%Ni to in situ synthesize $FeNi_3$ magnetic parts and showed that the magnetic properties can be altered by the prevalent laser parameters [31]. Dadbakhsh et al. investigated the in situ formation of Metal Matrix Composites during PBF-LB/M, stressing the need for small nanoparticles to create an effec-

tive reinforcement [32]. By adding CaB6 nanoparticles to 2024 aluminum alloy powder, the processability in PBF-LB/M was improved leading to crack-free and dense specimens with very small grains with high mechanical properties [33]. Adding pure copper (3%) to Ti6Al4V leads to intermetallic $CuTi_2$ precipitates through in situ alloying which increases the hardness and strength of the material [34]. Similar results were achieved by increasing the copper content to 5% and in addition, a correlation between applied volume energy density and resulting anisotropy was found [35]. Hentschel et al. used a direct energy deposition technique (LMD) to include carbon black nanoparticles in the tool steel AISI H11. Increasing the carbon content to more than 0.3 wt.% led to an increase in crack formation. The cracks could be reduced by implementing substrate pre-heating to 400 °C since the temperature is near or above the martensite start temperature of H11 [36]. By mixing pre-alloyed powders (316L with corrosion- and abrasion-resistant materials) in powder bed fusion using an electron beam unique tailored properties could be achieved [37]. Controlling the aluminum content in the X30Mn21 steel through powder blending and mixing in the PBF-LB/M process led to the ability to optimize the work-hardening behaviour through adjusting transformation-induced plasticity (TRIP) and twinning-induced plasticity (TWIP) [38]. In a review paper, Katz-Demyanetz et al. state promising possibilities to develop tailored material properties and the application for high entropy alloys (HEA). Although, the need for in-depth material studies is addressed [39]. Chen et al. fabricated a CoCrFeMnNi HEA through in situ alloying showing a homogeneous chemical distribution with an evaporation of Mn [40]. The use of a carbon-enriched paste in laser hardening was studied by Spira; this increased the case hardness of 16MnCr5 significantly [41]. In summary, it can be said that in situ alloying, especially with carbon, has a great potential to increase flexibility and alter material properties. However, choosing the right carbon particles and laser parameters to achieve fully dense parts is still a challenge. Additionally, further investigation is needed into the resulting microstructure and the process of carbon diffusion in rapid cooling processes like PBF-LB/M.

In this contribution the resulting microstructure when fabricating 16MnCr5 with PBF-LB/M is initially described with an analysis of the depletion of carbon that occurs during the process. Three carbon carrying powders are then presented and two are selected for the in situ alloying process. The resulting microstructure with a varying carbon content is described in detail for the most promising powder. Next, the final mechanical properties (hardness and tensile strength) in the as-built and in a heat-treated state are presented. Finally, there is a thorough discussion of the conducted research. The outlook presents the potential of multi-material parts in a gear section and summarizes the results.

2. Materials and Methods

An EOS M 290 machine (EOS GmbH, Krailingen, Germany) was used to manufacture the specimen. The maximum laser power of the ytterbium-fibre-laser is 400 W nominal laser power and the maximum scanning speed is 7 m/s. A carbon brush was used for recoating and a constant layer thickness of 30 µm with preheating to 80 °C was employed. Argon served as a shielding gas. A modified SLM 250HL machine (SLM Solution AG, Lübeck, Germany) was used to fabricate a gear segment with varying carbon content showing the possible freedom of functional graded materials in additive manufacturing [26]. The particle size distribution (PSD) of the powders was analysed by laser diffraction with a Mastersizer 3000 from Malvern Instruments (Worcestershire, UK). The microstructure was investigated using the Olympus BX53M optical microscope (Olympus Corporation, Shinjuku, Japan) and detailed images of the fracture surfaces were captured with a Hitachi TM3030Plus Tabletopscanning electron microscope (SEM, Hitachi High-Tech Corporation, Tokyo, Japan). Microstructure images were taken after etching for 30 s with 2% nitric acid (2% HNO_3). The hardness was tested (HV0.1 to HV10) using a Zwick Roell ZHU2.5 according to DIN EN ISO 6507-1. Tensile tests were carried out using a Zwick Roell Z050 (Zwick Roell, Ulm, Germany) according to DIN EN ISO 6892-1. The tensile specimens were in accordance with form E from DIN 50125. The chemical composition was analysed by

optical emission spectrometry (OES) and the carbon content was additionally determined by carrier gas hot extraction using a Leco CS-200 (Leco Corporation, St. Joseph, MI, USA). A Nabertherm annealing furnace N31 under argon atmosphere was used for the heat treatment. For the X-ray diffraction, an empyrean XRD Diffractometer using Co-tubing was used.

　　　Prealloyed 16MnCr5 (1.7131) powder is used as a basis. 16MnCr5 is a low alloyed steel with case hardening capabilities. It is widely used in drivetrain parts and especially in gears. The chemical composition of the powder can be seen in Table 1.

Table 1. Chemical composition of 16MnCr5 in wt.% (1) DIN EN10084 (2) supplier certificate and carrier hot gas extraction.

Elements	C	Mn	Cr	Si	P	S	Fe
(1)	0.14–0.19	1.0–1.3	0.8–1.1	$\leq$0.4	$\leq$0.025	$\leq$0.035	residual
(2)	0.15	1.05	0.9	0.19	-	-	residual

　　　The powder was atomized using argon gas and lies within the range specified in DIN EN 10084, whereby all main alloying elements are at the lower end of the tolerance. The lower carbon content could decrease the possibilities of cracks. However, even low element depletion has the possibility of leading to a part with a chemical composition that is out of the specification.

3. Results

3.1. Microstructure and Carbon Depletion of 16MnCr5

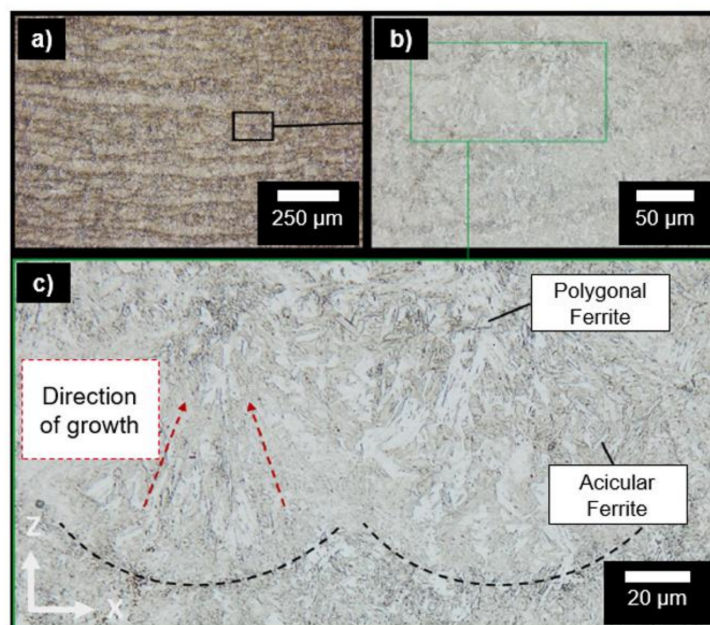　　　The microstructure in the as-built state after the PBF-LB/M process is shown in Figure 1.

Figure 1. Microstructure of as-built 16MnCr5 with z indicating the build direction of the PBF-LB/M process, (**a**) 100× magnification, (**b**) 500× magnification, (**c**) digital magnification.

　　　Parameters derived from earlier work that result in high part densities have been used to manufacture the specimens [6]. The horizontal and undulating weld tracks can be seen in Figure 1a. Following further magnification, the microstructure can be divided up into ferritic, bainitic and martensitic microstructure constituents. The ferritic structures can be split into polygonal and acicular ferrite. Polygonal ferrite, also called allotriomorphic ferrite, primarily forms at grain boundaries or inclusions through heterogeneous nucleation and has an amorphous shape with no crystallographic symmetry. In contrast, acicular

ferrite is produced at very fast cooling speeds, such as those experienced in PBF-LB/M, and is characterized by an arbitrary arrangement of small, needle-shaped ferrite plates. Acicular ferrite is preferable since its toughness can delay crack propagation [42]. Moreover, the dark areas are identified as a bainitic-martensitic mixed structure. Possible melt pool boundaries are marked in Figure 1c, showing a directed solidification in build direction (z-direction). Relatively small grain sizes can be seen in the proximity of the melt pool boundaries, whereas the more distant grains show an increased grain size, which may be attributed to different temperature gradients during the cooling phase.

Table 2 shows the chemical composition of the powder that was used and the resulting sample of 16MnCr5, combining OES (used for Mn and Cr) and hot carrier gas extraction (carbon content) measurements. It becomes clear that the sample has a low carbon and manganese content. 13% of carbon and 19% of manganese content are lost during the process, respectively. In contrast, the chromium content is slightly higher. The most likely explanation is that the elements are vaporized during the process due to the high energy input of the laser. Additionally, Zhao et al. suggest a reaction of carbon atoms with residual oxygen into carbon monoxides (CO) and dioxides (CO_2) at the melt pool surface, leading to the depletion of the carbon content [21].

Table 2. Comparison of chemical composition showing carbon depletion (1) powder, wt.% (2) build material, wt.% (3) percentage change; rem: remaining.

Elements	C	Mn	Cr	Si	P	S	Fe
(1)	0.15	1.05	0.9	0.19	-	-	residual
(2)	0.13	0.86	0.97	0.15	0.01	0.008	residual
(3)	−13%	−19%	+7%	−21%	-	-	-

The measured loss of carbon content lies within the range presented in the literature. If one applies Equation (1), the carbon loss of 0.02 wt.% results in a maximum loss of hardness of around 2.5 HRC, or roughly 50 HV. This may not seem much at first glance but becomes relevant if one considers the high demands of drivetrain applications. This may lead to a loss of certain critical properties required in the heat treatment process, especially considering the interdependency with the loss of manganese (reduction of critical cooling rate and increasing hardenability). In addition, the positive effects of manganese are decreased in terms of forgeability and weldability, which have a positive influence on the tensile and yield strength.

3.2. Carbon Particle Selection and Particle Size Distribution of Pre-Mixed Powders

To counteract the effect of carbon depletion and to allow the possibility of adjusting specific material properties, carbon particles are mixed with the pre-alloyed 16MnCr5 powder. Suitable powders containing carbon have to be identified beforehand. In this case, two graphite powders, both containing more than 99% carbon and a glassy carbon, are analysed. Glassy carbon is pure carbon that combines the properties of graphite and ceramics with a strongly disordered microstructure. The particle size distributions of the powders are shown in Figure 2, which indicates a bimodal distribution of graphite powder 1 with a high amount of particles with a size of around 10 μm. In contrast, graphite powder 2 has a very broad distribution. The 50%-quantile of the powders are 47 μm for the 16MnCr5 powder, 14 μm for graphite powder 1, 42 μm for graphite powder 2 and 30 μm for the glassy carbon powder (c.f. Table 3).
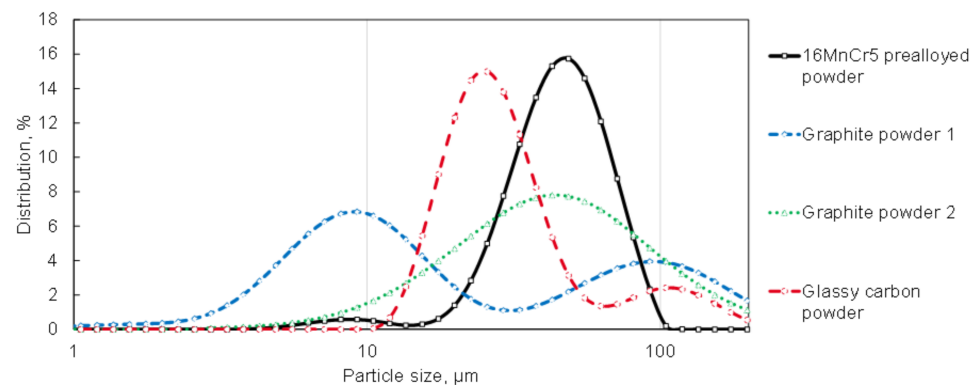
Figure 2. Particle size distribution of the powders used showing a narrow distribution of the glassy carbon powder.

Table 3. 10, 50, 90 %-quantile of the 16MnCr5, graphite and glassy carbon powder.

Powder	D10	D50	D90
16MnCr5	28 μm	47 μm	72 μm
Graphite 1	5 μm	14 μm	130 μm
Graphite 2	15 μm	42 μm	116 μm
Glassy Carbon	18 μm	30 μm	114 μm

None of the carbon-carrying powders have clear borders at the higher end of the distribution. They all contain large particles with sizes above 120 μm. A large share of fine particles is preferred for a homogenous distribution of the carbon particles in the 16MnCr5 powder.

The resulting powder mixtures are depicted in Figure 3, showing that the particles from graphite powder 2 are equal to or larger than the particles of the 16MnCr5 powder. The glassy carbon powder particles are significantly smaller and can mix well with nearly twice as large 16MnCr5 particles. Graphite powder 1 has the smallest particles, which are non-spherical but possess the ability to adhere to the 16MnCr5 particles, as can be seen in the magnification in Figure 3b.
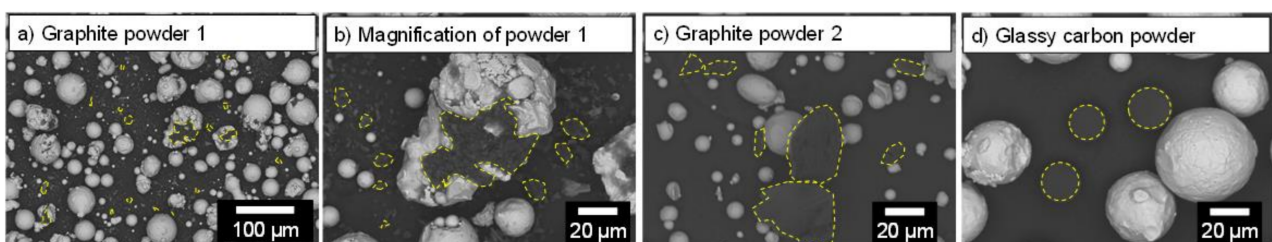

Figure 3. Powder mixtures of pre-alloyed 16MnCr5 powder with (**a**) graphite powder 1, (**b**) magnification of graphite powder 1, (**c**) graphite powder 2, (**d**) glassy carbon.

Graphite powder 1 and the glassy carbon powder are used in the further investigations. Graphite powder 2 is excluded on account of the large particles and the broad distribution, which are incompatible with the goal of a homogeneous particle mixture. A wheel mixer was used to mix the powders homogeneously and carbon particles were added to achieve carbon contents from 0.3 to 0.8 wt.% in the processed material. An analysis of the mixed powder showed that in addition to the 0.02 wt.% to counteract the depletion, 0.04 wt.% of carbon has to be added to achieve the nominal carbon content. Some of the graphite

powder, as well as the glassy carbon particles, stick to the container walls during the mixing process, leading to the additional loss of carbon during this process.

3.3. Processing by Powder Bed Fusion Using a Laser Beam

An EOS M290 machine was used to process the powder mixtures by means of PBF-LB/M, with process parameters at an energy density of 110 J/mm^3 [6]. No process-related disturbances such as excessive fume or spatter formation were observed. During the processing of the powder mixture with glassy carbon, non-dissolved particles could be observed in the top layers or when the energy input was reduced (c.f. Figure 4b).
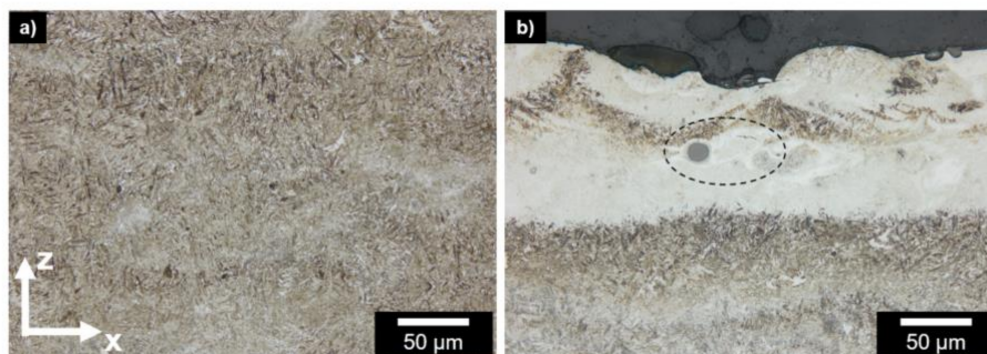

Figure 4. Comparison of resulting microstructure, (**a**) result with graphite powder 1 at 0.5 wt.% C, (**b**) result with glassy carbon powder at the top layer with marked particle and crack at 0.5 wt.% C; z indicates the build direction.

Microcracks were often found next to unmolten glassy carbon particles, indicating that the residual stresses exceed the yield strength of the material at this point. Since the unmolten particles only appeared in the top layers, re-melting and heating while processing the subsequent layers led to a homogeneous distribution and dissolution of the glassy carbon particles. When processing the powder mixtures with graphite powders, the graphite was dissolved without residue. Analysing the specimen revealed no cracks or pore formation. The resulting relative density of all specimens was over 99.8% and is shown in detail in Table 4. The carbon content does not influence the density, even if the carbon content reduces the weldability of steels.

Table 4. Resulting relative densities depending on the carbon content.

Carbon Content, wt.%	0.15	0.3	0.4	0.5	0.8
Relative density, %	99.93	99.89	99.91	99.91	99.84

Figure 5 shows the resulting microstructure of the specimen, whereby the proportion of martensite increases steadily while the bainitic and ferritic shares decline. At carbon contents between 0.15 wt.% and 0.4 wt.%, the microstructure is still ferritic (needle-like and polygonal).

In addition, fine structures can be found which correspond to bainite and possibly lancet martensite. Plate martensite can be detected for the first time as of 0.5 wt.% C, whereas ferritic components are now absent. Very low amounts of retained austenite are visible in the metallographic cross-sections. At 0.8 wt.% carbon content, an increasing amount of plate martensite is formed with a low retained austenite content. X-ray crystallography experiments on the specimens show the occurrence of a face-centred cubic phase above a carbon content of 0.5 wt.% (c.f. Figure 6). By applying the Rietvield-methode the retained austenite content can be estimated with 10% at 0.8 wt.% C. The emerging retained austenite content is comparable with the literature from case-hardened 16MnCr5 [43].
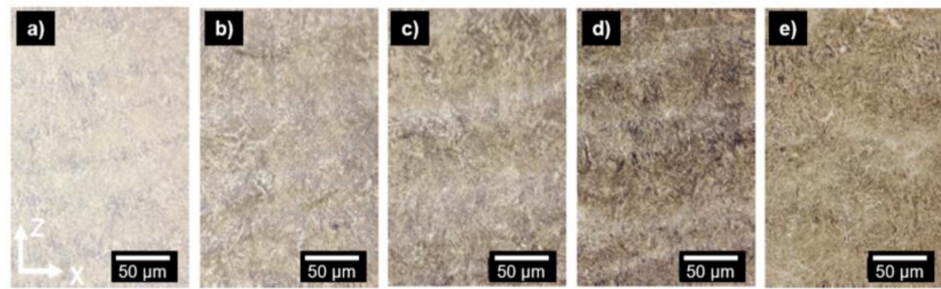
Figure 5. Microstructure depending on the carbon content achieved with graphite powder at 500×
magnification, (**a**) 0.15 wt.% C (reference), (**b**) 0.3 wt.% C, (**c**) 0.4 wt.% C, (**d**) 0.5 wt.% C, (**e**) 0.8 wt.% C.
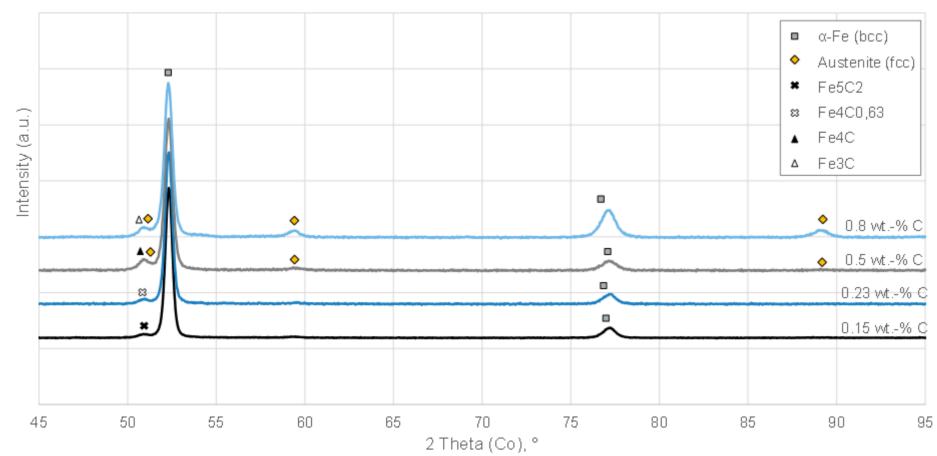

Figure 6. X-ray diffraction pattern at varied carbon content showing retained austenite at 0.8 wt.%
carbon content (bcc: body-centred cubic; fcc: face-centred cubic).

In addition to the X-ray diffraction, images of the specimen with 0.8 wt.% carbon
taken by light microscope and SEM are presented in Figure 7. The images confirm the
previous findings by revealing retained austenite and a mainly martensitic structure. The
SEM image provides evidence in presenting the formed carbides that were formed during
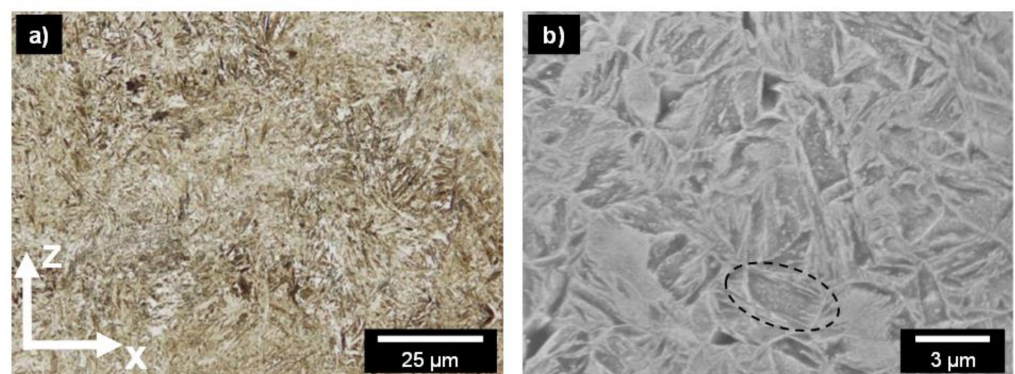the PBF-LB/M process.

Figure 7. Details of the 0.8 wt.% C specimen in the as-built state, (**a**) light microscope image
revealing fine martensite and retained austenite (**b**) SEM image showing carbides; z indicates the
build direction.

3.4. Mechanical Properties

The hardness of the specimens with varied carbon content is initially measured in the as-built state. The hardness at 0.15 wt.% C is 330 HV10 and rises slowly to 527 HV10 at 0.8 wt.% C (c.f. Figure 8). A good regression fit (coefficient of determination R^2 = 0.98) is achieved by a logarithmic approximation with the exact equation displayed in Figure 8. The increasing hardness corresponds to the change in microstructure from a ferritic to a more bainitic-martensitic composition. Nevertheless, for a bainitic-martensitic microstructure at 0.8 wt.%, the hardness of 527 HV10 is relatively low which is caused by the amount of retained austenite.
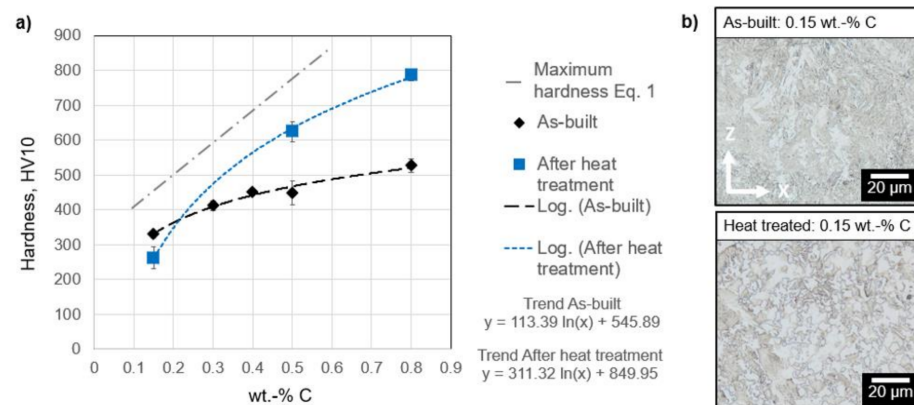

Figure 8. (**a**) Hardness measurements in the as-built and heat-treated state. Hardness after PBF-LB/M is higher before a heat treatment for low carbon content (**b**) Microstructure of 16MnCr5 with 0.15 wt.% C before and after heat treatment.

Furthermore, these hardness values differ significantly from the maximum achievable hardness, which can be calculated using Equation (1). Subsequently, heat treatment is carried out at the case hardening temperature of 16MnCr5 with quenching (heating at 870 °C for 50 minutes with subsequent oil quenching). The hardness values for higher carbon contents increase significantly whereas the hardness of the low carbon content decreases even further from 330 HV10 to 261 HV10 (−21%). A higher ferrite content and a different ferrite morphology can be observed in the microscope images in part (b) of Figure 8 for the 0.15 wt.% carbon state after heat treatment. Martensitic fractions do not occur here because of the comparatively low cooling rates and low carbon content. In addition to the higher ferrite content, the microstructure after heat treatment is much more coarse. The changed morphology, as well as the more coarse microstructure, are possible causes for the decrease in hardness. The hardness increases from 450 to 620 HV10 (+37%) at 0.5 wt.% and changes from 527 to 786 HV10 (+49%) at 0.8 wt.%. A regression fit (coefficient of determination R^2 = 0.99) is achieved by a logarithmic approximation. After heat treatment, the maximum nominal hardness (c.f. Equation (1)) is almost reached in the 0.3 to 0.5 wt.% carbon content range. The intersection of the two logarithmic regressions is located at a carbon content of 0.215 wt.% and a hardness of around 370 HV10.

The hardness and the microstructure give a good impression of the nature of the resulting material. Nevertheless, the state of residual stress or the ductility are vital properties and the tensile tests that are performed offer more insights into the material. The specimens were printed in a horizontal position facing downwards, as indicated in Figure 9, and the samples were tested in the as-built state. The specimens show a plastic deformation and necking at 0.15 wt.% C. The tensile and yield strength are very close together and an ideal elastic-plastic behaviour can be observed. The corresponding fracture surface in Figure 9b show microscopically recognizable honeycombs which are typical for a ductile fracture. The samples with 0.5 wt.% carbon content showed the highest tensile strength of 1438 N/mm^2 and a yield strength of 1330 N/mm^2. The analysis of the fracture

surface reveals a mixed fracture surface with fracture honeycombs and transcrystalline fracture surfaces. A further increase in carbon content leads to a decrease in strength and ductility. The samples break without necking and the fracture surfaces show typical signs of transcrystalline fractures. With an increasing carbon content, the elongation at fracture decreases steadily. In contrast, the strength is highest at 0.5 wt.% C and decreases at 0.8 wt.% C. In a trade-off between strength and ductility, the samples produced with 0.5 wt.% C possess the highest strength while maintaining medium ductility.
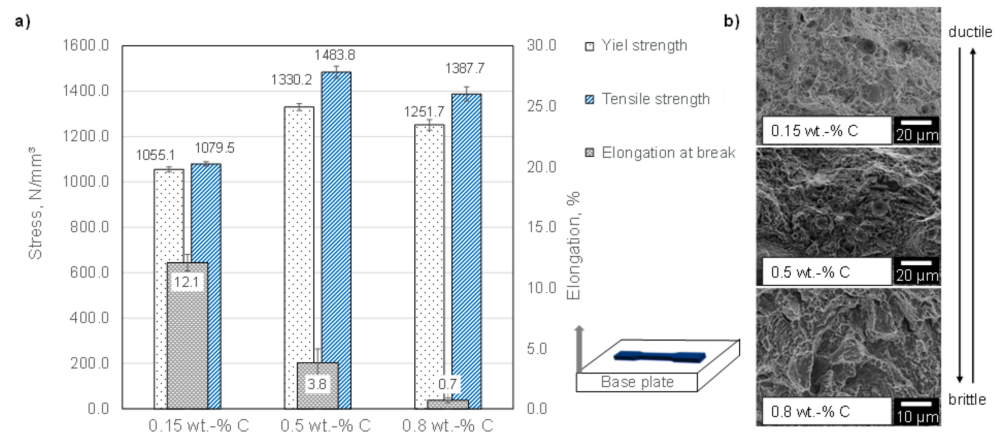

Figure 9. (**a**) Results of the tensile tests showing the strength-ductility trade-off with a varied carbon content; the arrow indicates the build direction (**b**) Fracture surfaces of the corresponding specimen changing from ductile to brittle behaviour with an increased carbon content.

4. Discussion

The formation of the resulting microstructure in the as-built state is closely connected to the melt pool behaviour and cooling rates. The largest temperature difference occurs at the melt pool boundaries. This means that the highest cooling rates can be expected here because of heat conduction to solid material. Strong subcooling causes a high nucleation rate, resulting in a finely structured microstructure. A diffusion-free folding process with bainite and martensite formation is the logical consequence. Further solidification moves in the direction of the melt pool centre. The temperature gradient between the melt and the already solidified material decreases, and with it the cooling rate. Consequently, increasingly ferritic and coarser structures can form in the melt pool centre. This mechanism describes a single exposure and does not consider the layer-by-layer structure of the PBF-LB/M process. The temperature input of the subsequent layers affects the microstructure that has already formed through tempering effects such as carbon partitioning or grain coarsening. Nevertheless, the fine microstructure at the melt pool boundaries prevails.

The depletion of chemical elements during the PBF-LB/M process with pre-alloyed powders must occur during the coupling of heat from the laser into the powder bed and the formation of the melt pool. Sublimation is possible due to the rapid input of heat. The melting point of manganese is 1519 K, with an evaporation temperature of 2334 K, whereas graphite melts at 3813 K, evaporates at 5100 K and pure carbon's sublimation point is at 3915 K. Melt pool measurements by Hooper on Ti-6Al-4V show that temperatures of well above 3000 K occur for hatch scans with peaks of over 4000 K during turns at the end of scan lines [13]. Considering the lower laser power applied for Ti-6Al-4V, similar or even higher temperatures have to be expected when processing 16MnCr5. This allows the manganese to melt, which promotes the reaction with residual oxygen in the build chamber or the direct sublimation. This can also be observed when welding high manganese steels [44]. Simulation results for the melt pool formation of 316L show that the evaporation temperature of sulphide (>3200 K) is reached in a small area of the melt pool at laser powers above 200 W [45]. This can promote the evaporation of manganese and the reaction of liquefied carbon with the residual oxygen in the build chamber.

The added graphite particles are fully absorbed and the microstructures show no signs of carbon aggregations. The Marangoni convection in the melt pool leads to a homogeneous distribution of carbon, promoting a good mixture in the melt pool and thus leading to the development of the homogenous microstructure [46]. It would also appear that the carbon has diffused since no aggregations are seen. This diffusion takes place during the first rapid cooling of the melt pool or re-heating when processing subsequent layers. The glassy carbon particles are not dissolved in the top layers, indicating that the repeated heating of 16MnCr5 in the PBF-LB/M process is more likely to cause the glassy carbon to diffuse and spread. For this distribution to occur and for the glassy carbon to dissolve completely, a high energy input and several melting processes are necessary. The use of graphite with small particles is recommended for further studies since the glassy carbon is not fully dissolvable and micro-cracks occurred. This difference can be linked to the difference in the crystalline structure of graphite (hexagonal planes) and the unsorted amorphous structure of glassy carbon. A higher energy is needed to break the amorphous structure, whereas only weak Van der Waals connections between the planes have to be broken in the graphite.

The hardness measurements reveal that fine grains with a mostly ferritic and bainitic microstructure are formed during the PBF-LB/M process at low carbon contents, which become coarser during the heat treatment and lead to a decrease in hardness. At higher carbon contents, the as-built state has a lower hardness compared to the heat-treated state which is in accordance with the amount of retained austenite found in the as-built state. Additionally, a thermal cycle of cooling and re-heating takes place during the PBF-LB/M process. This in situ heat treatment leads to tempering effects and favours the formation of precipitates at the grain boundaries. In addition, an effect due to coarsening can also be assumed, since a martensite needle originally has a high dislocation density due to the high cooling rate. A high dislocation density can act as a driving force for recrystallization [47]. The retained austenite and these effects decrease the hardness in the as-built state.

Tensile tests showed that the yield and tensile strength is highest at 0.5 wt.% C, combined with a medium elongation at fracture. Adding further carbon particles does not improve the strength but does decrease the ductility significantly. Martensite forms after heat treatment (heating and quenching) with high carbon contents. The tempering effects of the PBF-LB/M process are eliminated and a higher hardness can be achieved.

The in situ alloying approach is very suitable for PBF-LB/M. Further powder bed based additive manufacturing technologies like binder jetting or electron beam melting could also benefit within certain limits. Due to the vacuum chamber in electron beam melting less element depletion due to reactions with residual oxygen in the build chamber is presumable. The high powder bed temperatures would lead to a higher diffusion of the carbon decreasing multi-material capabilities. On the other hand, even higher carbon contents could be processed with the high preheating temperatures. The difference in as-built and quenched hardness would increase since a lower temperature gradient during the process is present. In situ alloying could also be used in binder jetting. However, the recoating with a roller could lead to adhesion of the carbon particles and thus segregation of the powder mixture. The high temperatures and long process time during sintering would increase the diffusion of carbon, limiting parts with a defined carbon gradient. After sintering, quenching would be necessary to achieve full hardness.

5. Summary and Outlook

The microstructure of 16MnCr5 processed via PBF-LB/M is presented in detail and the resulting carbon and manganese depletion are quantified. Adding carbon particles to pre-alloyed 16MnCr5 powder is one way to counteract this effect. Altering the carbon content is also a suitable strategy to adapt the microstructure and the mechanical properties of parts. Processing the powder mixture with an increased carbon content does not lower the relative densities that are achieved. Glassy carbon particles are less suitable than graphite powder because micro-cracks occur close to non-dissolving particles of glassy carbon in top layers. Depending on the carbon content, the microstructure changes from ferritic-bainitic

at 0.15 wt.% to bainitic-martensitic at 0.8 wt.%. The most balanced mechanical properties in the as-built state are achieved at a carbon content of 0.5 wt.%. During subsequent heat treatment (heating and quenching), the microstructure becomes more coarse with low carbon contents, which in turn decreases the hardness. With higher carbon contents, the retained austenite and the tempering effects that occur during the thermal cycle in the PBF-LB/M process are eliminated and the hardness increases significantly.

The possibility of quickly altering the steel composition by adding carbon opens up new opportunities in the development of alloys for additive manufacturing and could shorten development cycle times and reduce costs. Furthermore, new possibilities arise when considering multi-material processing in additive manufacturing. Materials with high carbon content and increased hardness can be used in wear-affected zones, whereas the nominal material can be used in the remaining part for good dynamic and ductile fatigue properties. No additional carburization process would be required for case hardening steels if carbon-enriched powders could be deposited during the PBF-LB/M process. The freedom offered by PBF-LB/M means that parts with varying case hardening depth (c.f. Figure 10; pores originating from faulty contour scan) are possible or even structures with high intrinsic strength. In addition, the use of lattice structures or minimum surface areas bodies, e.g., gyroids is possible. Global case hardening of such structures would lead to an embrittlement and weaken the part's overall integrity. Combined with the design approach of ultralight components by replicating lattice structures in different sizes and order of magnitude, highly optimized and extreme lightweight parts for demanding applications like energy or aerospace could be produced [48].
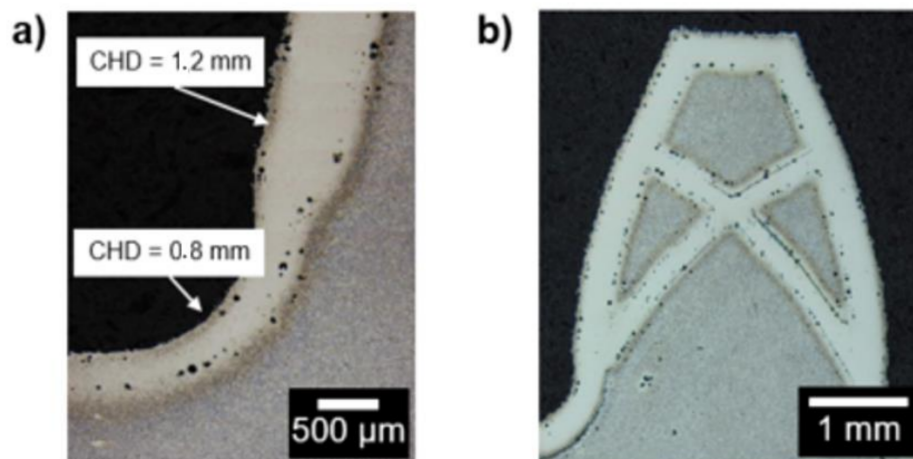

Figure 10. Potential of the combination of in situ alloying and multi-material processing (**a**) Tooth with various case hardening depths produced with multi-material PBF-LB/M (**b**) Tooth with inherent pressure-resistant zones of high strength material.

Future work should explore the effects of in situ alloying with different elements such as manganese or wear-resistant components such as tungsten carbides. These elements have different alloying characteristics since no, or much less diffusion is possible compared to carbon. Additionally, the multi-material process has to be improved to take full advantage of in situ alloying. Furthermore, powder recycling has to be addressed as a key point. Up to now, the graphite particles cannot be separated from the original powder to create a new powder batch.

Author Contributions: Conceptualization, M.S., J.W. and G.S.; Data curation, M.S., A.G. and U.T.; Formal analysis, M.S., A.G. and J.W.; Investigation, M.S., A.G. and U.T.; Supervision, T.T., K.S., J.S. and G.R.; Validation, M.S.; Writing—original draft, M.S.; Writing—review and editing, A.G., J.W., T.T., G.S., K.S., U.T., J.S. and G.R. All authors have read and agreed to the published version of the manuscript.

Data Availability Statement: The raw/processed data required to reproduce these findings cannot be shared at this time as the data also forms part of an ongoing study.

References

1. Thompson, M.K.; Moroni, G.; Vaneker, T.; Fadel, G.; Campbell, R.I.; Gibson, I.; Bernard, A.; Schulz, J.; Graf, P.; Ahuja, B.; et al. Design for Additive Manufacturing: Trends, opportunities, considerations, and constraints. *CIRP Ann.* **2016**, *65*, 737–760. [CrossRef]
2. Kranz, J.; Herzog, D.; Emmelmann, C. Design guidelines for laser additive manufacturing of lightweight structures in TiAl6V4. *J. Laser Appl.* **2015**, *27*, S14001. [CrossRef]
3. VDI-Fachbereich Produktionstechnik und Fertigungsverfahren. 2014. VDI-Richtlinie 3405. Available online: https://www.vdi.de/richtlinien/details/vdi-3405-additive-fertigungsverfahren (accessed on 23 March 2021).
4. Lutter-Guenther, M.; Seidel, S.; Kamps, T.; Reinhart GLutter-Guenther, M.; Seidel, S.; Kamps, T.; Reinhart, G. Imple-mentation of Additive Manufacturing Business Models. *Appl. Mech. Mater.* **2015**, *794*, 547–554. [CrossRef]
5. Herzog, D.; Seyda, V.; Wycisk, E.; Emmelmann, C. Additive manufacturing of metals. *Acta Mater.* **2016**, *117*, 371–392. [CrossRef]
6. Schmitt, M.; Schlick, G.; Seidel, C.; Reinhart, G. Examination of the processability of 16MnCr5 by means of laser powder bed fusion. *Procedia CIRP* **2018**, *74*, 76–81. [CrossRef]
7. Niemann, G.; Winter, H. *Maschinenelemente: Band 2: Getriebe Allgemein, Zahnradgetriebe—Grundlagen, Stirnradgetriebe, Zweite, Völlig Neubearbeitete Auflage Ed*; Springer: Berlin/Heidelberg, Germany, 2003; 376p.
8. Conrado, E.; Gorla, C.; Davoli, P.; Boniardi, M. A comparison of bending fatigue strength of carburized and nitrided gears for industrial applications. *Eng. Fail. Anal.* **2017**, *78*, 41–54. [CrossRef]
9. Kamps, T.; Reinhart, G. *Increasing Transmission Efficiency by Implementation of a Conformal Cooling System Using Additive Manufacturing*; Fraunhofer: Berlin, Germany, 2014.
10. Ziebura, D.; Meiners, W. *Verarbeitung von Einsatz- und Vergütungsstählen Mittels SLM*; Fraunhofer ILT: Aachen, Germany, 2016; 1p.
11. Kluge, M.; Kotthoff, G.; Cavallini, C.; Höges, S. Design and Production of Innovative Transmission Com-Ponents with Additive Manufacturing. In Proceedings of the 16th International CTI Symposium Automotive Transmissions, HEV and EV Drives, Berlin, Germany, 4–7 December 2017.
12. Kamps, T. *Leichtbau von Stirnzahnrädern aus Einsatzstahl Mittels Laserstrahlschmelzen*; Technical University Munich: Munich, Germany, 2018; 199p.
13. Hooper, P.A. Melt pool temperature and cooling rates in laser powder bed fusion. *Addit. Manuf.* **2018**, *22*, 548–559. [CrossRef]
14. Beer, O.; Merklein, C.; Gerhard, D.; Hentschel, O.; Rasch, M.; Schmidt, M. Processing of the Heat Resistant Bearing Steel M50NiL by Selective Laser Melting. *HTM J. Heat Treat. Mater.* **2018**, *73*, 187–201. [CrossRef]
15. Siglmueller, F.; Kupfer, S.; Kamps, T.; Schmitt, M.; Lohner, T.; Reinhart, G.; Stahl, K. Efficiency of Additive Manufactured Gears with Conformal Cooling. In Proceedings of the 21st TAE International Colloquium Tribology, Stuttgart, Germany, 9–11 January 2018.
16. Schmitt, M.; Jansen, D.; Bihlmeir, A.; Winkler, J.; Anstaett, C.; Schlick, G.; Tobie, T.; Stahl, K.; Reinhart, G. Framework and strategies for the lightweight construction of AM gears for the au-tomotive industry. *Proc. RapidTech* **2019**. [CrossRef]
17. Rehme, O. Cellular Design for Laser Freeform Fabrication. Ph.D. Dissertation, Technical University Hamburg-Harburg, Hamburg, Germany, 2009; 150p.
18. Nakamoto, T.; Shirakawa, N.; Miyata, Y.; Inui, H. Selective laser sintering of high carbon steel powders studied as a function of carbon content. *J. Mater. Process. Technol.* **2009**, *209*, 5653–5660. [CrossRef]
19. Taha, M.A.; Yousef, A.F.; Gany, K.A.; Sabour, H.A. On selective laser melting of ultra high carbon steel: Effect of scan speed and post heat treatment. *Mater. Werkst.* **2012**, *43*, 913–923. [CrossRef]
20. Jelis, E.; Clemente, M.; Kerwien, S.; Ravindra, N.M.; Hespos, M.R. Metallurgical and Mechanical Evaluation of 4340 Steel Produced by Direct Metal Laser Sintering. *JOM* **2015**, *67*, 582–589. [CrossRef]
21. Zhao, X.; Song, B.; Zhang, Y.; Zhu, X.; Wei, Q.; Shi, Y. Decarburization of stainless steel during selective laser melting and its influence on Young's modulus, hardness and tensile strength. *Mater. Sci. Eng. A* **2015**, *647*, 58–61. [CrossRef]
22. Liedtke, D. Über den Zusammenhang zwischen dem Kohlenstoffgehalt in Stählen und der Härte des Martensits. *Mater. Werkst.* **2003**, *34*. [CrossRef]
23. Prinz, C.; Clausen, B.; Hoffmann, F.; Kohlmann, R.; Zoch, H.-W. Metallurgical influence on distortion of the case-hardening steel 20MnCr5. *Mater. Werkst.* **2006**, *37*, 29–33. [CrossRef]
24. Tobie, T. Zur Grübchen- und Zahnfußtragfähigkeit Einsatzgehärteter Zahnräder. Ph.D. Dissertation, Technical University Munich, Munich, Germany, 2001; 215p.

25. Mosallanejad, M.H.; Niroumand, B.; Aversa, A.; Saboori, A. In-situ alloying in laser-based additive manufacturing processes: A critical review. *J. Alloys Compd.* **2021**, *872*, 159567. [CrossRef]

26. Anstaett, C.; Seidel, C.; Reinhart, G. Fabrication of 3D-Multi-Material Parts by Laser Beam Based Powder Bed Fusion. Solid Freeform Fabrication 2017. In Proceedings of the 28th Annual International Solid Freeform Fabrication Symposium, Austin, TX, USA, 7–9 August 2017.

27. Sing, S.; Huang, S.; Goh, G.; Tey, C.; Tan, J.H.K.; Yeong, W. Emerging metallic systems for additive manufacturing: In-situ alloying and multi-metal processing in laser powder bed fusion. *Prog. Mater. Sci.* **2021**, *119*, 100795. [CrossRef]

28. Murali, K.; Chatterjee, A.; Saha, P.; Palai, R.; Kumar, S.; Roy, S.; Mishra, P.; Choudhury, A. Direct selective laser sintering of iron–graphite powder mixture. *J. Mater. Process. Technol.* **2003**, *136*, 179–185. [CrossRef]

29. Simchi, A.; Pohl, H. Direct laser sintering of iron–graphite powder mixture. *Mater. Sci. Eng. A* **2004**, *383*, 191–200. [CrossRef]

30. Kruth, J.P.; Froyen, L.; van Vaerenbergh, J.; Mercelis, P.; Rombouts, M.; Lauwers, B. Selective laser melting of iron-based powder. *J. Mater. Process. Technol.* **2004**, *149*, 616–622. [CrossRef]

31. Zhang, B.; Fenineche, N.-E.; Liao, H.; Coddet, C. Magnetic properties of in-situ synthesized $FeNi_3$ by selective laser melting Fe-80%Ni powders. *J. Magn. Magn. Mater.* **2013**, *336*, 49–54. [CrossRef]

32. Dadbakhsh, S.; Mertens, R.; Hao, L.; van Humbeeck, J.; Kruth, J.-P. Selective Laser Melting to Manufacture "In Situ" Metal Matrix Composites: A Review. *Adv. Eng. Mater.* **2019**, *21*, 1801244. [CrossRef]

33. Mair, P.; Goettgens, V.S.; Rainer, T.; Weinberger, N.; Letofsky-Papst, I.; Mitsche, S.; Leichtfried, G. Laser powder bed fusion of nano-CaB6 decorated 2024 aluminum alloy. *J. Alloys Compd.* **2021**, *863*, 158714. [CrossRef]

34. Vilardell, A.; Takezawa, A.; du Plessis, A.; Takata, N.; Krakhmalev, P.; Kobashi, M.; Albu, M.; Kothleitner, G.; Yadroitsava, I.; Yadroitsev, I. Mechanical behavior of in-situ alloyed Ti6Al4V(ELI)-3 at.% Cu lattice structures manufactured by laser powder bed fusion and designed for implant applications. *J. Mech. Behav. Biomed. Mater.* **2021**, *113*, 104130. [CrossRef] [PubMed]

35. Mosallanejad, M.; Niroumand, B.; Aversa, A.; Manfredi, D.; Saboori, A. Laser Powder Bed Fusion in-situ alloying of Ti-5%Cu alloy: Process-structure relationships. *J. Alloys Compd.* **2021**, *857*, 157558. [CrossRef]

36. Hentschel, O.; Siegel, L.; Scheitler, C.; Huber, F.; Junker, D.; Gorunow, A.; Schmidt, M. Processing of AISI H11 Tool Steel Powder Modified with Carbon Black Nanoparticles for the Additive Manufacturing of Forging Tools with Tailored Mechanical Properties by Means of Laser Metal Deposition (LMD). *Metals* **2018**, *8*, 659. [CrossRef]

37. Koptyug, A.; Popov, V.V.; Botero Vega, C.A.; Jiménez-Piqué, E.; Katz-Demyanetz, A.; Rännar, L.-E.; Bäckström, M. Compositionally-tailored steel-based materials manufactured by electron beam melting using blended pre-alloyed pow-ders. *Mater. Sci. Eng. A* **2020**, *771*, 138587. [CrossRef]

38. Köhnen, P.; Ewald, S.; Schleifenbaum, J.H.; Belyakov, A.; Haase, C. Controlling microstructure and mechanical prop-erties of additively manufactured high-strength steels by tailored solidification. *Addit. Manuf.* **2020**, *35*, 101389.

39. Katz-Demyanetz, A.; Koptyug, A.; Popov, V.V. In-situ Alloying as a Novel Methodology in Additive Manufac-Turing. In *Proceedings of the 2020 IEEE 10th International Conference Nanomaterials: Applications & Properties (NAP), Sumy, Ukraine, 9–13 November 2020*; IEEE: Piscataway, NJ, USA, 2020.

40. Chen, P.; Yang, C.; Li, S.; Attallah, M.M.; Yan, M. In-situ alloyed, oxide-dispersion-strengthened CoCrFeMnNi high entropy alloy fabricated via laser powder bed fusion. *Mater. Des.* **2020**, *194*, 108966. [CrossRef]

41. Spira, C. *Erweiterung der Prozessgrenzen Von Laserbasierten Härteverfahren im Automotive-Bereich*; Technical University Dresden: Dresden, Germany, 2016; 178p.

42. Schulze, G. *Die Metallurgie des Schweissens: Eisenwerkstoffe—Nichteisenmetallische Werkstoffe, 4., Neu Bearbeitete Aufl. Ed*; Springer: Heidelberg, Germany; New York, NY, USA, 2010; 614p.

43. Burkart, K.; Bomas, H.; Zoch, H.-W. Fatigue of notched case-hardened specimens of steel SAE 5120 in the VHCF re-gime and application of the weakest-link concept. *Int. J. Fatigue* **2011**, *33*, 59–68. [CrossRef]

44. Dahmen, M.; Lindner, S.; Monfort, D.; Petring, D. Weld Metallurgy and Mechanical Properties of High Manganese Ultra-high Strength Steel Dissimilar Welds. *Phys. Procedia* **2016**, *83*, 344–351. [CrossRef]

45. Le, T.-N.; Lo, Y.-L. Effects of sulfur concentration and Marangoni convection on melt-pool formation in transition mode of selective laser melting process. *Mater. Des.* **2019**, *179*, 107866. [CrossRef]

46. Martin, A.A.; Calta, N.P.; Hammons, J.A.; Khairallah, S.A.; Nielsen, M.H.; Shuttlesworth, R.M.; Sinclair, N.; Matthews, M.J.; Jeffries, J.R.; Willey, T.M.; et al. Ultrafast dynamics of laser-metal interactions in additive manufacturing alloys captured by in situ X-ray imaging. *Mater. Today Adv.* **2019**, *1*, 100002. [CrossRef]

47. Hengsbach, F.; Koppa, P.; Duschik, K.; Holzweissig, M.J.; Burns, M.; Nellesen, J.; Tillmann, W.; Tröster, T.; Hoyer, K.-P.; Schaper, M. Duplex stainless steel fabricated by selective laser melting—Microstructural and mechanical properties. *Mater. Des.* **2017**, *133*, 136–142. [CrossRef]

48. Calleja-Ochoa, A.; Gonzalez-Barrio, H.; de Lacalle, N.L.; Martínez, S.; Albizuri, J.; Lamikiz, A. A New Approach in the Design of Microstructured Ultralight Components to Achieve Maximum Functional Performance. *Materials* **2021**, *14*, 1588. [CrossRef]